Supporting information for manuscript

Asymmetric [Dy_2] molecules deposited into micro-SQUID susceptometers: in-situ characterization of their magnetic integrity

Ana Repollés,[a,†] María Carmen Pallarés,[a,b,†] David Aguilà,[c,d] Olivier Roubeau,[a] Verónica Velasco,[c,d] Diego Gella,[a] Leoní A. Barrios,[c,d] María José Martínez-Pérez,[a] Javier Sesé,[a] Dietmar Drung,[e] Jesús Ignacio Martínez,[a] Thomas Schurig,[e] Boris Le Guennic,[f] Anabel Lostao,[a,b,g] Guillem Aromí,[c,d] and Fernando Luis[a]

[a]*Instituto de Nanociencia y Materiales de Aragón (INMA), CSIC and Universidad de Zaragoza, Plaza San Francisco s/n, 50009 Zaragoza, Spain. Email: fluis@unizar.es*
[b]*Laboratorio de Microscopias Avanzadas (LMA), Universidad de Zaragoza, 50018 Zaragoza, Spain*
[c]*Departament de Química Inorgànica i Orgànica, Universitat de Barcelona, Diagonal 645, 08028 Barcelona, Spain. E-mail: aromi@ub.edu*
[d]*Institut of Nanoscience and Nanotechnology of the University of Barcelona (IN2UB), Barcelona, Spain.*
[e]*Physikalisch-Technische Bundesanstalt (PTB), Abbestraße 2-12, D-10587 Berlin, Germany*
[f]*Univ Rennes, CNRS, ISCR (Institut des Sciences Chimiques de Rennes) - UMR 6226, F-35000 Rennes, France*
[g]*Fundación ARAID, 50018 Zaragoza, Spain*

Table of contents

1. Supporting figures and tables
1.1. Table S1. Crystallographic and refinement parameters for **[Dy_2]** and **[LaDy]**
1.2. Table S2. Coordination environment of the Dy sites in **[Dy_2]** and **[LaDy]**
1.3. Table S3. Details of H-bonding in **[Dy_2]** and **[LaDy]**
1.4. Figure S1. View of the structure of **[Dy_2]** with labelled atoms
1.5. Figure S2. View of the structure of **[LaDy]** with labelled atoms
1.6. Figure S3. Mass spectra of **[Dy_2]** and **[LaDy]**
1.7. Figure S4. UV-visible absorption spectra for solutions of **[Dy_2]**: stability in solution
1.8. Figure S5. Controlled patterning of **[Dy_2]** nano- and micro-deposits by means of DPN nanolithography
1.9. Figure S6. Integration of **[Dy_2]** deposits onto μ-SQUID susceptometers
1.10. Figure S7. Image of a bulk **[Dy_2]** sample on a μ-SQUID susceptometer.
1.11. Figure S8. Magnetic susceptibility of bulk **[LaDy]** and **[Dy_2]**.
1.12. Figure S9. Specific heat of bulk **[LaDy]** and **[Dy_2]**.
1.12. Figure S10. Imaginary magnetic susceptibilities of bulk **[LaDy]** and **[Dy_2]** samples and of **[Dy_2]** deposits.
1.13. Figure S11. Simulated EPR spectra and energy levels for a **[Dy_2]** molecule at different magnetic field orientations
2. Ab-initio calculation of spin states and single-ion magnetic anisotropies in **[LaDy]** and **[Dy_2]**
3. Numerical simulations of the magnetic flux generated by **[Dy_2]** arrays deposited onto μ-SQUID sensors.
4. References

1. Supporting tables and figures

Table S1. Crystallographic and refinement parameters for **[Dy_2]** and **[LaDy]**.

Compound	**[Dy_2]**	**[LaDy]**
Crystal size (mm^3)	0.12x0.10x0.09	0.23x0.05x0.02
Formula	$C_{55}H_{37}ClDy_2N_5O_{15}$, 3($C_5H_5N$), C_5H_6N	$C_{50}H_{35}DyLaN_5O_{19}$, 4($C_5H_5N$), C_5H_6N
FW (g mol^{-1})	1685.75	
Wavelength (Å)	0.71073	0.71073
Crystal system	monoclinic	monoclinic
Space group	$P2_1/n$	$P2_1/n$
Z	4	4
T (K)	150(2)	150(2)
a (Å)	12.7916(4)	14.533(4)
b (Å)	16.6444(4)	15.8767(13)
c (Å)	32.5450(10)	32.939(4)
β (°)	97.104(3)	91.083(15)
V ($Å^3$)	6875.9(3)	7599(2)
ρ_{calcd} (g cm^{-3})	1.628	1.593
μ (mm^{-1})	2.271	1.612
Independent reflections	9873 (R_{int} = 0.1261)	6864 (R_{int} = 0.1282)
restraints / parameters	102 / 919	359 / 937
Goodness-of-fit on F^2	1.026	1.010
Final R_1 / wR_2 [$I>2\sigma(I)$]	0.0578 / 0.0976	0.0611 / 0.1160
Final R_1 / wR_2 [all data]	0.1056 / 0.1126	0.1285 / 0.1535
largest diff. peak and hole (e $Å^3$)	1.031 / –0.757	0.862 / –0.789

Table S2. Metal–ligand bond distances (Å) and metal···metal separations (Å) in the structures of compounds **[Dy_2]** and **[LaDy]**.

[Dy_2]		**[LaDy]**	
Dy1–O3	2.301(6)	Dy1–O11	2.358(10)
Dy1–O11	2.310(6)	Dy1–O9	2.373(10)
Dy1–O9	2.343(6)	Dy1–O4	2.436(11)
Dy1–O8	2.398(5)	Dy1–O19	2.444(10)
Dy1–O4	2.405(6)	Dy1–O8	2.450(10)
Dy1–O13	2.416(6)	Dy1–O13	2.453(8)
Dy1–N3	2.490(7)	Dy1–N3	2.482(11)
Dy1–N4	2.633(8)	Dy1–N5	2.711(12)
Dy1–N5	2.653(8)	La2–O14	2.478(10)
Dy2–O6	2.363(6)	La2–O1	2.495(10)
Dy2–O1	2.371(6)	La2–O6	2.506(9)
Dy2–O13	2.385(6)	La2–O13	2.543(9)
Dy2–O14	2.404(6)	La2–O3	2.583(9)
Dy2–O3	2.494(6)	La2–N1	2.641(13)
Dy2–O8	2.518(6)	La2–O16	2.648(10)
Dy2–N1	2.534(7)	La2–O8	2.683(9)
Dy2–N2	2.537(7)	La2–N2	2.740(12)
Dy2–Cl1	2.725(2)	La2–O17	2.807(12)
Dy1···Dy2	3.7748(6)	Dy1···La2	3.8845(11)

Table S3. Details of H-bonding interactions in the structures of compounds **[Dy_2]** and **[LaDy]**.

D–H···A	D–H (Å)	H···A (Å)	D–A (Å)	D–H···A (º)
[Dy_2]				
N1S–H1S···O1	0.88	2.23	2.940(12)	137.6
N1S–H1S···O1	0.88	2.15	2.924(12)	146.9
[LaDy]				
N1S–H1SB···O1	0.88	3.11	3.527(19)	111.1
O19–H19C···N2S	0.90(2)	2.02(4)	2.771(17)	141(6)
O19–H19D···N3S	0.90(2)	2.02(4)	2.745(16)	138(6)

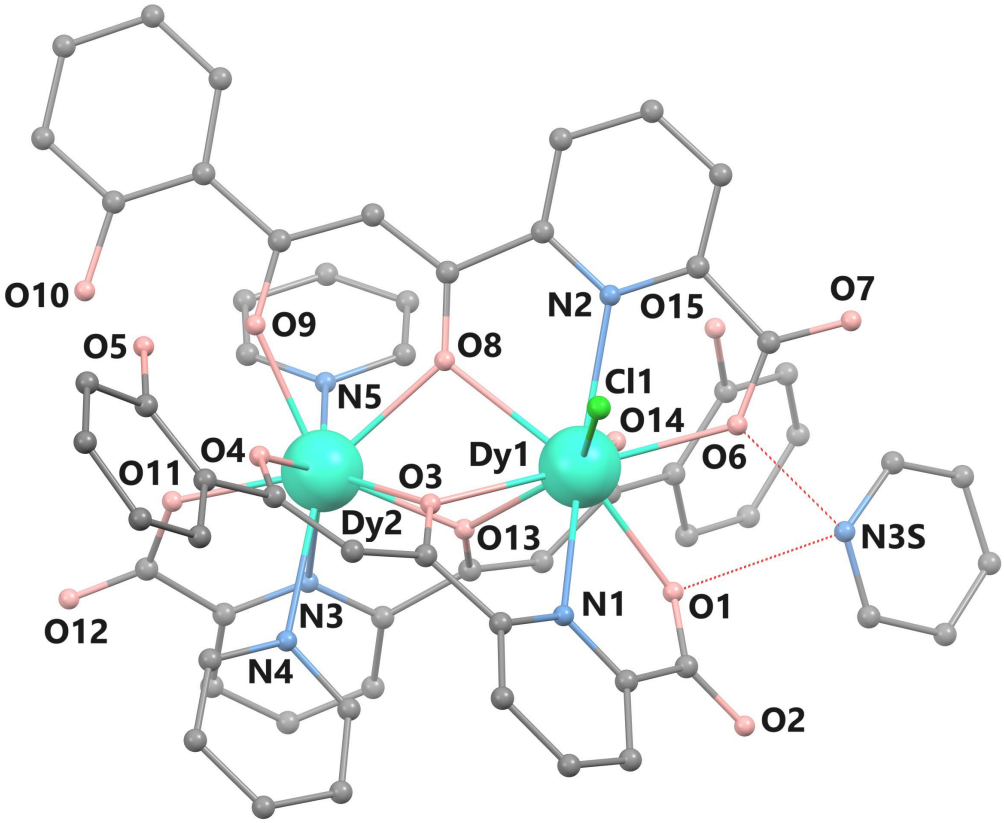

Figure S1. Molecular structure of **[Dy_2]** with heteroatoms labelled. Green is Dy, grey is C, salmon is O, blue is N. Hydrogen atoms are omitted for simplicity. Hydrogen bonds between Hpy^+ and the complex shown as are dashed red lines.

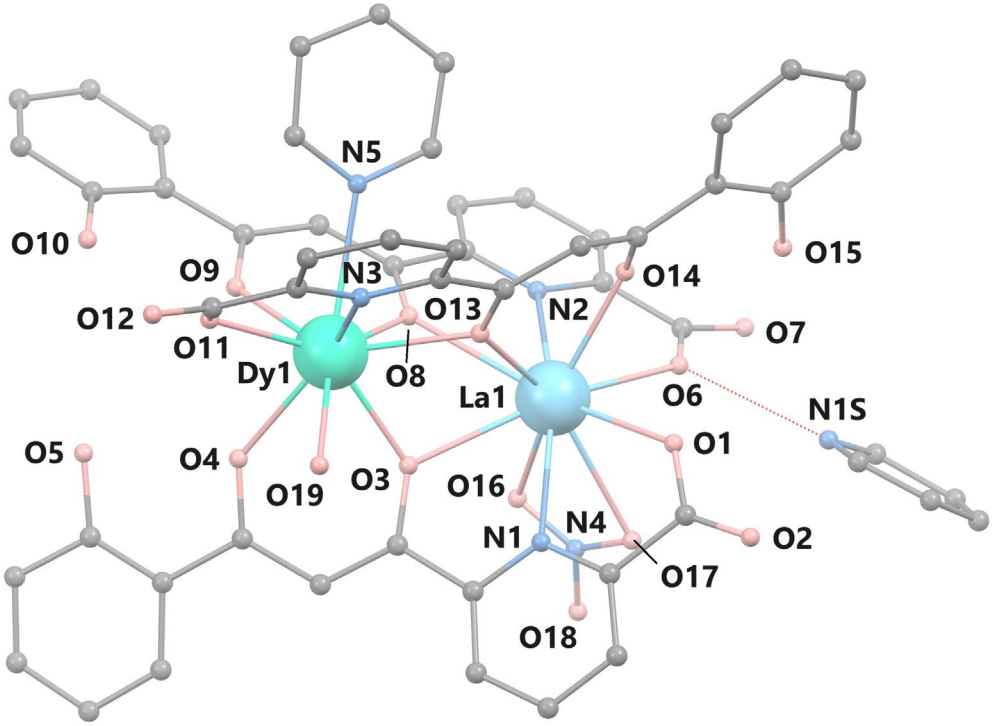

Figure S2. Molecular structure of **[LaDy]** with heteroatoms labelled. Green is Dy, light blue is La, grey is C, salmon is O, blue is N. Hydrogen atoms are omitted for simplicity. Hydrogen bonds between Hpy^+ and the complex shown as are dashed red lines.

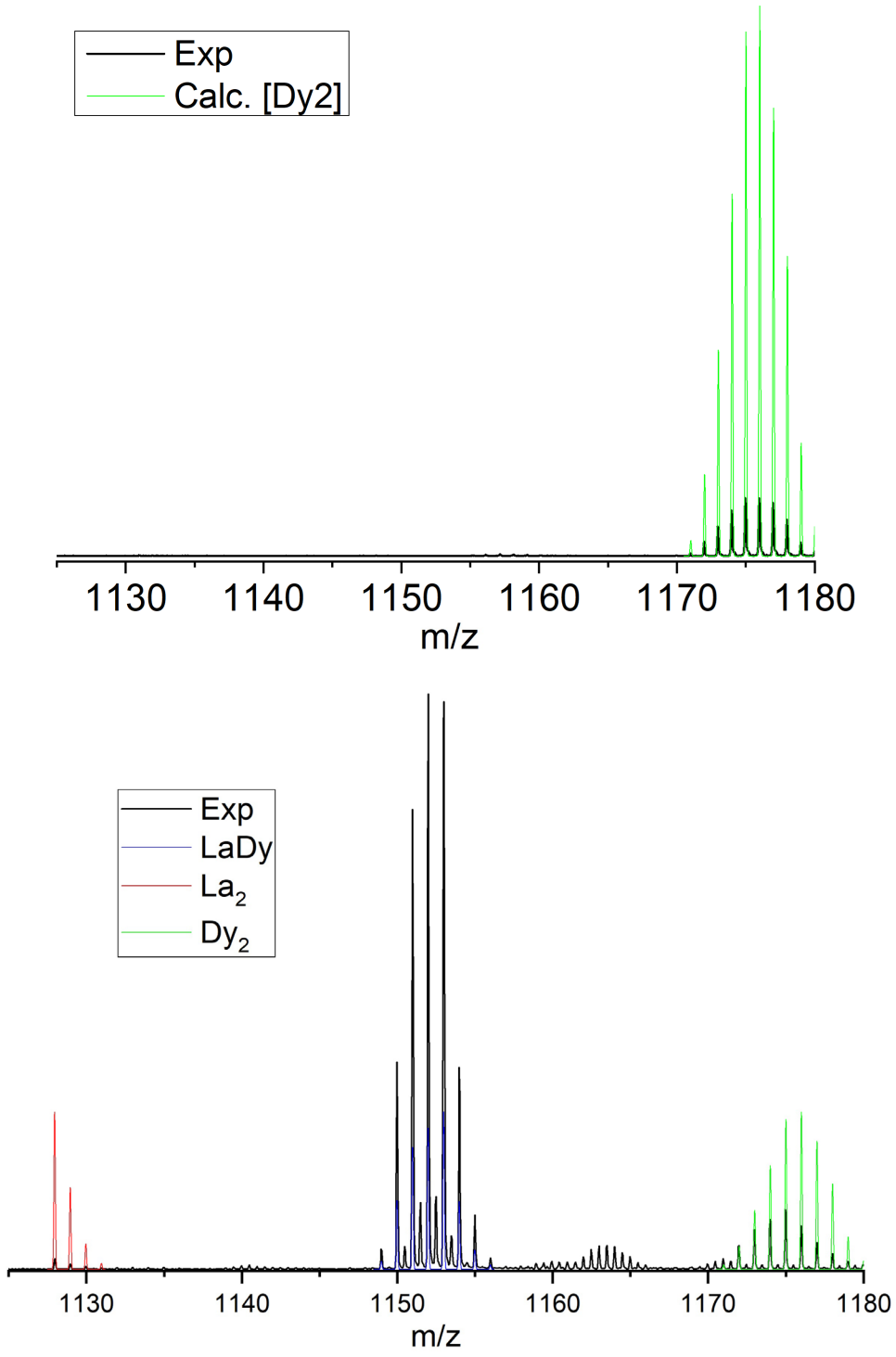

Figure S3. Top: Selected region of the experimental (black line) MALDI-TOF spectrogram of compound **[Dy$_2$]**, emphasizing the simulated ([$Dy_2(HL)_3$] + H^+)$^+$ (*m*/*z* = 1176.1010) fragment (green line). Bottom: Selected region of the experimental (black line) ESI-MS spectrogram of compound **[LaDy]**, emphasizing the simulated ([$LaDy(HL)_3$] + H^+)$^+$ (*m*/*z* = 1151.9956) fragment (blue line), together with the corresponding calculated signals for the **[Dy$_2$]** (green line) and **[La$_2$]** (red line), metal distributions. The minor traces of the homometallic moieties are due to scrambling taking place in the required methanol solution used for the mass spectrometry experiments (see also the bottom panel in Fig. S4 below).

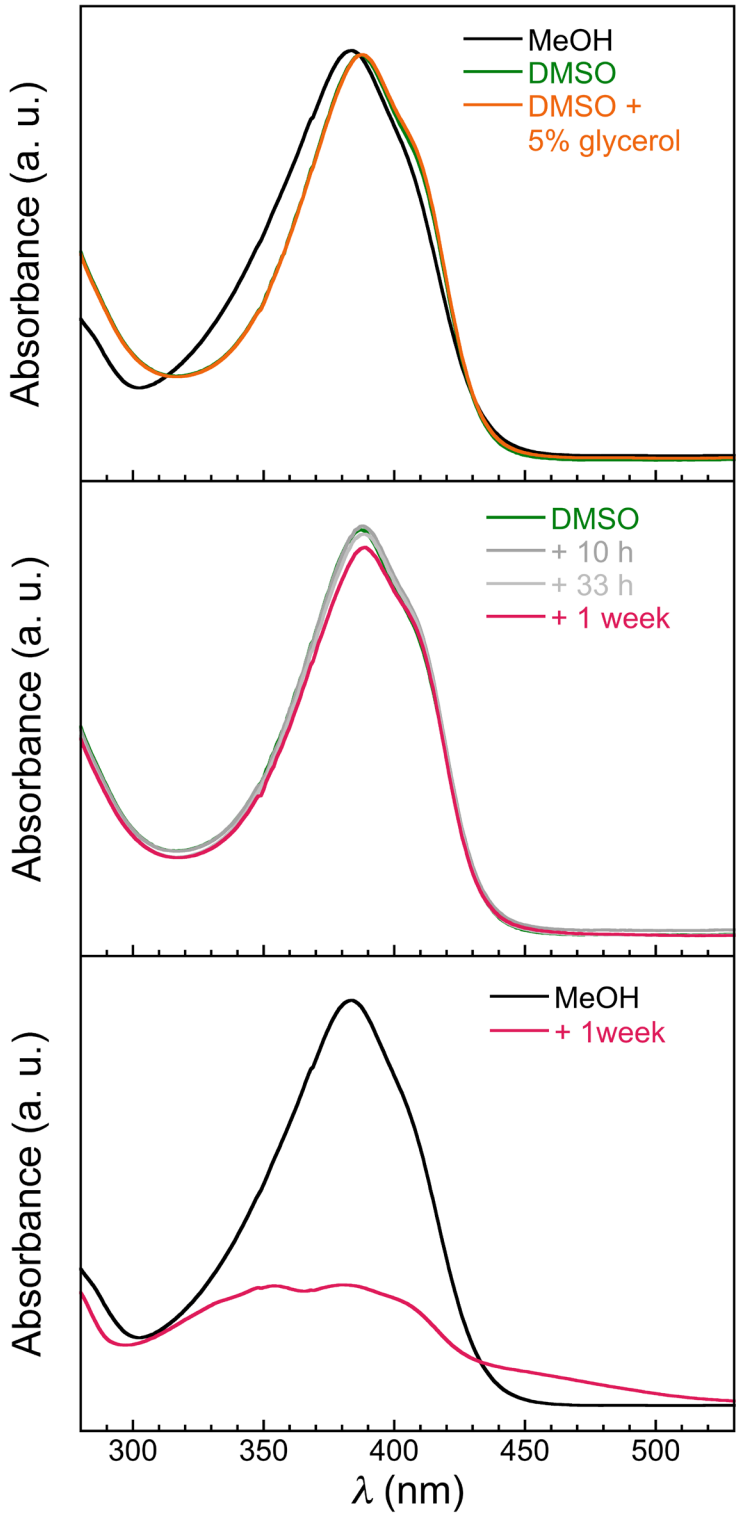

Figure S4. UV-visible absorption spectra for solutions of **[Dy_2]**: top, comparison of solutions in MeOH, DMSO and DMSO + 5% glycerol as indicated; middle and bottom, ageing of DMSO and MeOH solutions, respectively. “a.u” means arbitrary units.

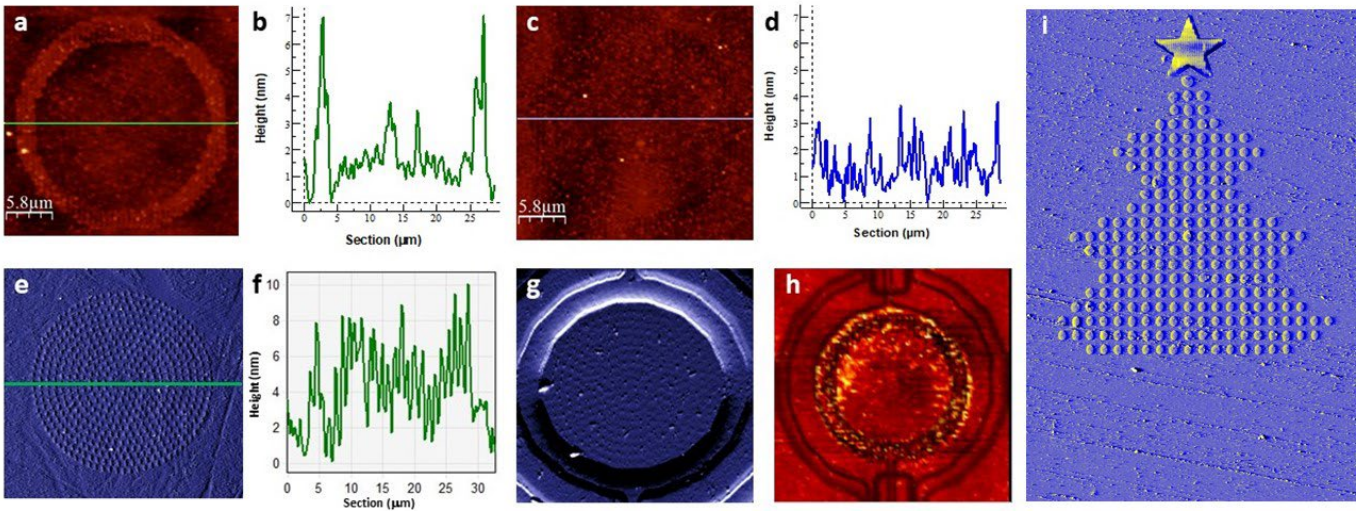

Figure S5. Controlled patterning of **[Dy_2]** nano- and micro-deposits by means of DPN nanolithography. a) AFM image of a 5-layer ring of **[Dy_2]** molecules patterned onto a silicon substrate. b) Height profile measured along the green line in the sample shown in a). c) AFM image of the same ring fabricated under the same experimental conditions as those used in a) with an ink that contains only the solvent and glycerol (i.e., no **[Dy_2]** molecules). d) Height profile measured along the blue line in the sample shown in c) showing that there is hardly any residue of glycerol. e) AFM 3-D topography image of a circle made of 5 nm (approximately 3 molecular layers) thick **[Dy_2]** dots, as shown in f) height profile corresponding to the green line exhibited in e). g) AFM 3-D topography image of the same pattern as in e) integrated inside the micro-SQUID pick-up coil. h) AFM 3-D topography image of 5-layer **[Dy_2]** dots patterned to form a ring next to the inner side of the micro-SQUID pickup coil under the same conditions as those used for a). i) Christmas tree fabricated organizing 5 nm thick **[Dy_2]** trilayers in 1.5 μm^2 wide dots. The star is a continuous 10 nm thick nanolitography.

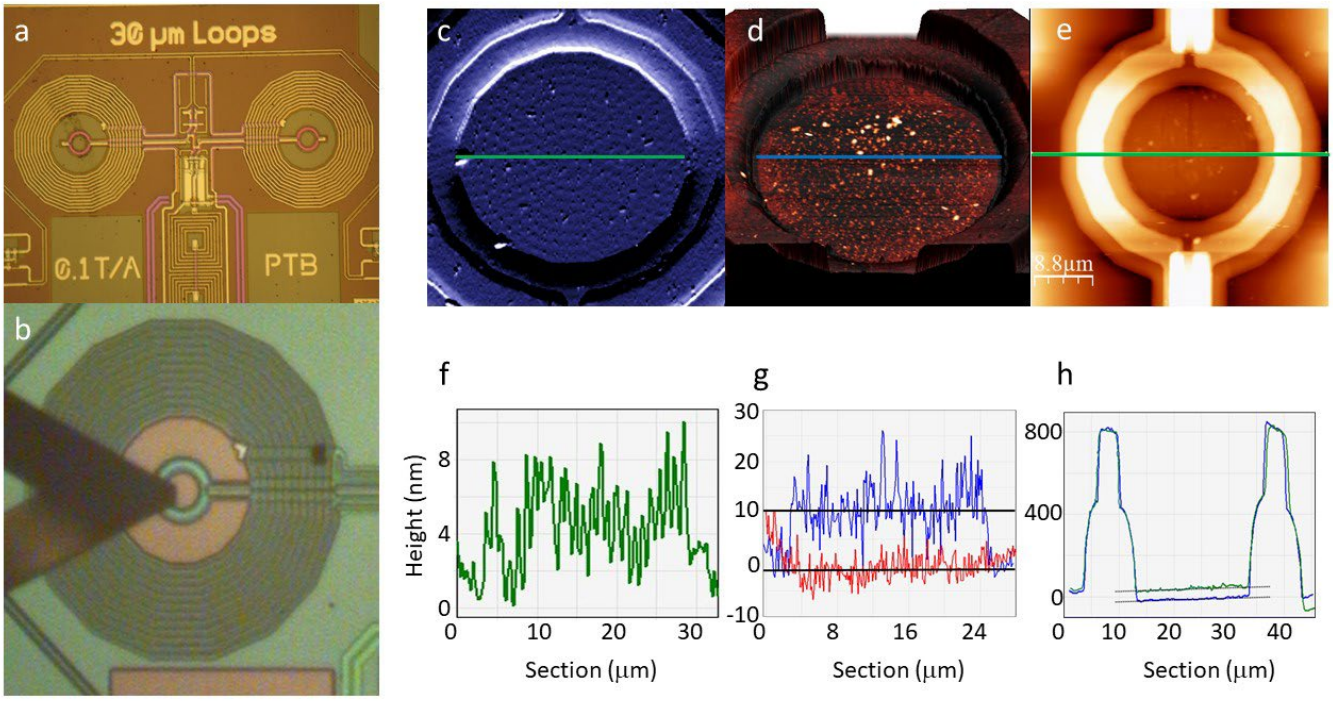

Figure S6. Integration of **[Dy$_2$]** deposits onto micro-SQUID susceptometers. (a) The micro-SQUID is made of two loops (coloured in magenta) with a gradiometric design, which act as pick-up coils. They are surrounded by two identical excitation coils that generate the ac magnetic field, perpendicular to the chip's surface. (b) Image of the AFM tip of the DPN system traversing the area defined by one of the two pick-up coils during one of the deposition processes. (c-e) and (f-h) Topography images (top) and height profiles along the corresponding lines at the top images (bottom) of three molecular deposits labelled as **[Dy$_2$]$_{DPN1}$** (c,f), **[Dy$_2$]$_{DPN2}$** (d,g) and **[Dy$_2$]$_{DPN3}$** (e,h). In (g) and (h) the lines below represent the profile of the substrate. The samples were made by successive coating and deposition steps. In the bigger samples, the large volume of the dots makes them merge on the substrate, forming a continuous thin film that covers the entire coil. Thus, deposition of approximately 3, 8 and 34 molecular layer thick deposits, were achieved respectively. The estimated number of **[Dy$_2$]** molecules transferred to the device is 2.3×10^8, 1.8×10^9 and 7×10^9, respectively.

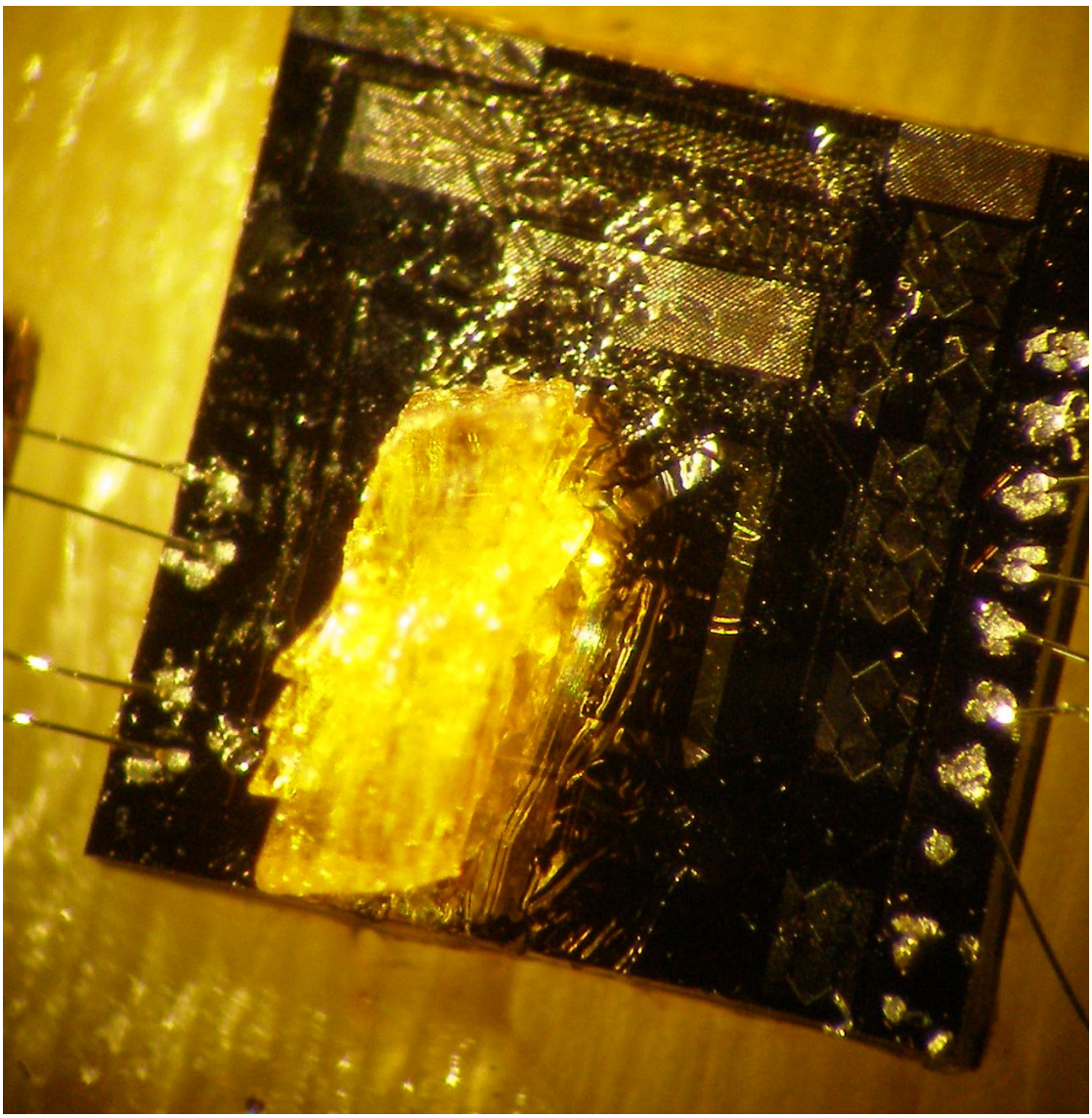

Figure S7. Optical microscopy image of a micro-SQUID susceptometer hosting a bulk **[Dy_2]** sample on one of its 800×400 μm^2 banana-shaped pick-up and excitation coils.

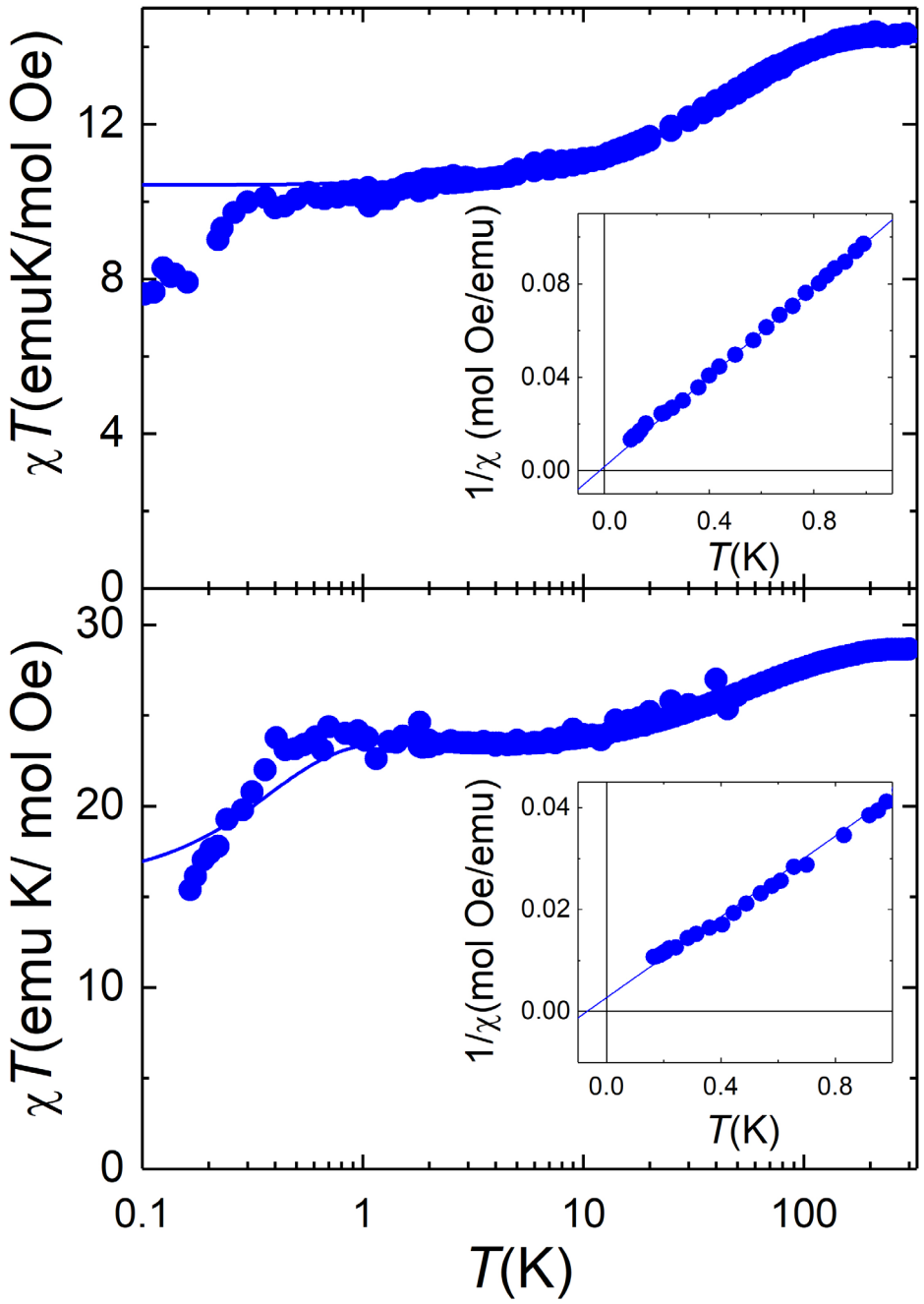

Figure S8. Comparison between the χT products of bulk **[LaDy]** (top panel) and **[Dy$_2$]** (bottom panel). The data have been extracted from the magnetic susceptibility measured at sufficiently low frequencies and sufficiently high temperatures to be considered as the equilibrium linear response of each sample. The insets show the reciprocal equilibrium susceptibility measured below T = 1 K (solid dots) and the Curie-Weiss fit (solid lines). The Weiss temperatures, which characterize the typical strength of spin-spin interactions, are θ = -0.015(5) K for **[LaDy]** and θ = -0.067(1) K for **[Dy$_2$]**.

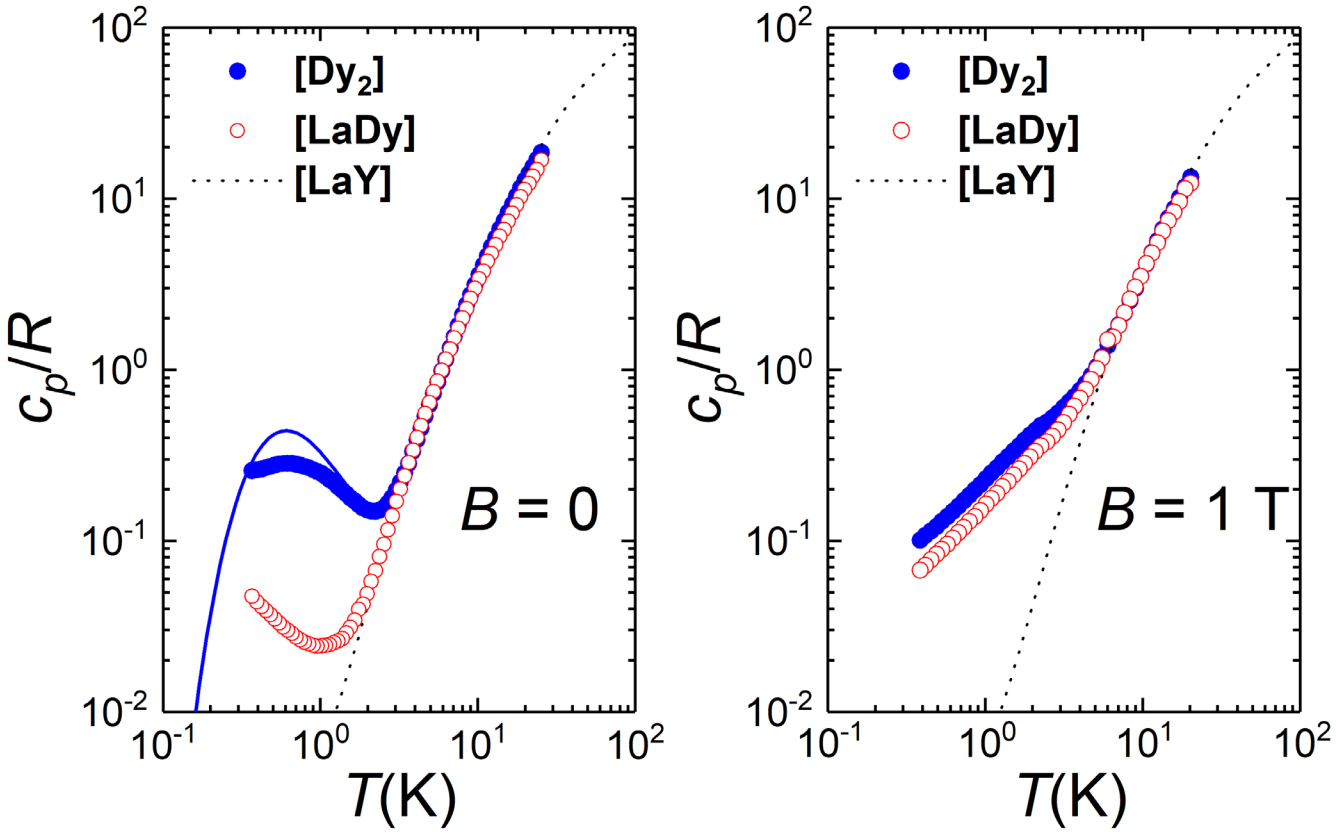

Figure S9. Comparison between the molar specific heat measured at zero magnetic field (left panel) and under a 1 T magnetic field (right panel) on bulk **[LaDy]** and **[Dy₂]** samples. Data measured on the diamagnetic **[LaY]** complex, which provides an estimation of the lattice contribution to c_P/R, are also shown as a dotted line. The solid line on the left hand side panel is a theoretical prediction based on the Hamiltonian (2) of the main text. The Schottky-like anomaly observed in the specific heat of **[Dy₂]**, and absent for **[DyLa]**, can be associated to the magnetic coupling between the two Dy(III) ions. The difference between c_P of the two molecular complexes tends to vanish as the magnetic field dominates over the effect of intra-molecular spin-spin interactions.

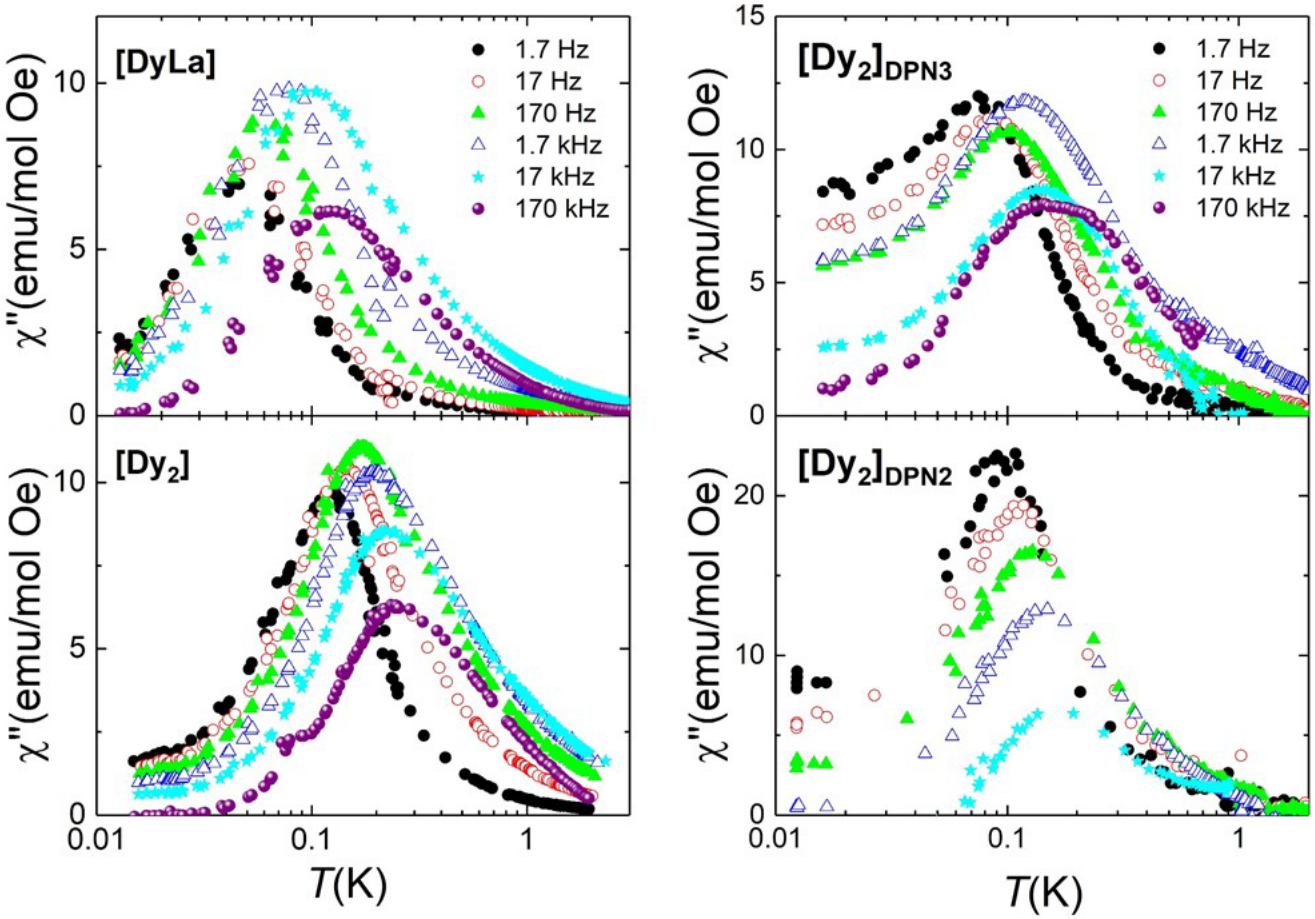

Figure S10. Imaginary component of the ac linear magnetic susceptibility of bulk **[LaDy]** and **[Dy$_2$]** (left), and of two **[Dy$_2$]** arrays deposited by DPN onto a micro-SQUID sensor (right) measured for different frequencies $\omega/2\pi$ of the excitation magnetic field. The maxima signal the condition $\omega\tau = 1$, with τ the characteristic spin relaxation time [1]. The data shown in Fig. 5 of the main text were obtained from these results. At any temperature, the relaxation time of all **[Dy$_2$]** samples is slower than that of **[LaDy]** (as evidenced by their χ" maxima occurring at higher *T* for the same ω), which shows that spin-spin interactions within each molecule hinder the spin reversal processes.

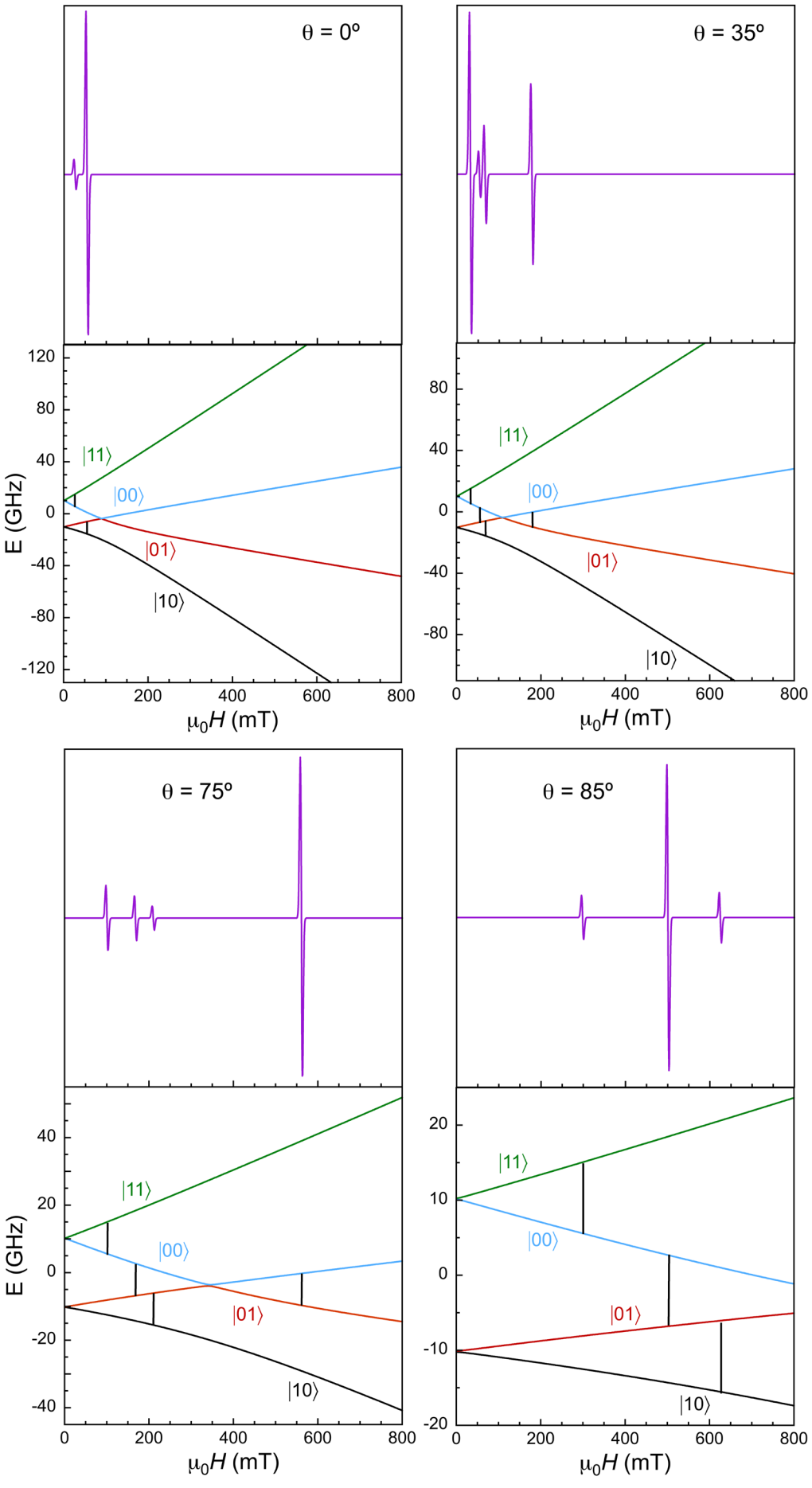
θ = 0°
θ = 35°
θ = 75°
θ = 85°
E (GHz)
μ0H (mT)
|11⟩
|00⟩
|01⟩
|10⟩

Figure S11. Simulated EPR spectra and energy levels schemes of an isolated **[Dy_2]** molecule for different magnetic field orientations as indicated. Simulations were done with Easyspin [2] using the same spin Hamiltonian parameters as for the bulk EPR spectrum and an hypothetic *P*1 single crystal, *i.e.* a unique **[Dy_2]** molecule. Theta is the angle between the z axis of the molecular frame, *i.e.* the anisotropy axis of Dy_1 site, and the magnetic field vector. Vertical bars indicate the expected transitions.

2. Ab-initio calculation of spin states and single-ion magnetic anisotropies in [LaDy] and [Dy_2]

[LaDy]

The calculations confirm the high magnetic anisotropy of the Dy center in **[LaDy]**. The wavefunction of the ground state consists of almost pure $|M_J\rangle = |\pm 15/2\rangle$, well separated (118 cm^{-1}) from the first excited state (mainly $|M_J\rangle = |\pm 13/2\rangle$ but with some contributions of $|\pm 7/2\rangle$ and $|\pm 11/2\rangle$) (Table S4). Additionally, the ground state *g* tensor is found to be highly anisotropic ($g_x = 0.1$, $g_y = 0.1$, $g_z = 19.3$). The ground state magnetic anisotropy axis is shown in Figure S12.

Table S4. Computed energies levels (the ground state is set at zero), component values of the Lande factor *g* and wavefunction composition for each M_J state of the ground-state multiplet for the Dy center in **[LaDy]**.

	E (cm^{-1})	g_x	g_y	g_z	WFT
1	0.0	0.1	0.1	19.3	$0.93\|\pm 15/2\rangle$
2	117.8	1.4	3.0	13.7	$0.58\|\pm 13/2\rangle + 0.19\|\pm 7/2\rangle + 0.11\|\pm 11/2\rangle$
3	169.7	0.5	3.3	9.9	$0.22\|\pm 9/2\rangle + 0.21\|\pm 5/2\rangle + 0.21\|\pm 11/2\rangle + 0.12\|\pm 3/2\rangle$
4	217.3	1.0	1.5	15.6	$0.50\|\pm 11/2\rangle + 0.28\|\pm 13/2\rangle$
5	249.5	0.1	2.3	10.6	$0.56\|\pm 9/2\rangle + 0.16\|\pm 7/2\rangle + 0.08\|\pm 11/2\rangle$
6	299.8	0.5	3.1	7.2	$0.42\|\pm 7/2\rangle + 0.26\|\pm 5/2\rangle + 0.17\|\pm 1/2\rangle$
7	338.6	10.5	8.0	2.8	$0.44\|\pm 3/2\rangle + 0.33\|\pm 5/2\rangle + 0.15\|\pm 1/2\rangle$
8	409.5	0.2	0.5	19.1	$0.48\|\pm 1/2\rangle + 0.28\|\pm 3/2\rangle + 0.12\|\pm 5/2\rangle$

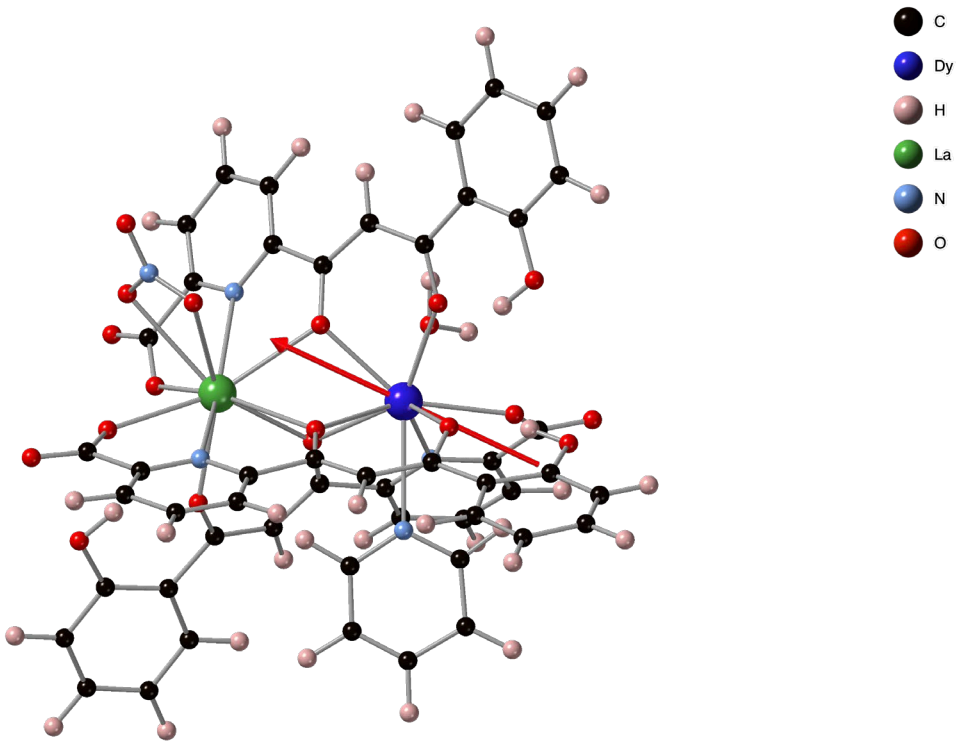

Figure S12. Anisotropy axis of the Dy(III) ion in **[LaDy]**.

[Dy_2]

For **[Dy_2]**, two separate calculations (replacing the second Dy(III) ion by a Y(III) ion) have been realized to get the magnetic properties of each Dy(III) center. In the calculations, Dy_1 corresponds to the Dy center bearing the Cl atom. The difference between both Dy ions is indeed clearly visible in the following tables. Dy_2 is much more Ising than Dy_1 with a *g* tensor close to what is expected for a pure $|M_J\rangle = |\pm 15/2\rangle$ ground-state ($g_x = g_y = 0$; $g_z = 19.4$). This is confirmed by the ground-state wavefunction that is also well separated (132 cm^{-1}) from the first excited state (mainly $|M_J\rangle = |\pm 13/2\rangle$) (Table S6).

The situation is markedly different for Dy_1 for which the ground-state anisotropy is much less axial (Table S5). The first excited state lies only 54 cm^{-1} higher in energy. This explains the important mixing observed in the wavefunctions, and point to different static magnetic properties.

The magnetic axes are far to be collinear (Figure S13) with the axis on Dy_2 oriented in a similar way as in **[LaDy].** The angle $\delta = 72^{\circ}$ has been obtained from the scalar product of both axes. Their different orientations are explained by the electrostatic distributions around the Dy(III) ions that are different in both cases.

Table S5. Computed energies levels (the ground state is set at zero), component values of the Lande factor *g* and wavefunction composition for each M_J state of the ground-state multiplet for Dy_1 center in **[Dy_2]**.

	E (cm^{-1})	g_x	g_y	g_z	WFT
1	0.00	0.1	0.3	18.2	0.66|±15/2⟩ + 0.18|±11/2⟩ + 0.13|±13/2⟩
2	53.5	0.4	0.9	16.4	0.69|±13/2⟩ + 0.13|±15/2⟩ + 0.09|±9/2⟩
3	91.9	0.1	1.6	17.0	0.25|±1/2⟩ + 0.24|±3/2⟩ + 0.19|±5/2⟩ + 0.11|±7/2⟩
4	137.8	2.2	4.1	11.7	0.43|±11/2⟩ + 0.14|±9/2⟩ + 0.13|±15/2⟩ + 0.12|±3/2⟩ + 0.12|±1/2⟩
5	176.0	1.7	5.8	10.8	0.23|±9/2⟩ + 0.21|±1/2⟩ + 0.21|±5/2⟩ + 0.13|±3/2⟩ + 0.09|±7/2⟩
6	223.1	2.4	4.1	10.1	0.36|±7/2⟩ + 0.18|±9/2⟩ + 0.15|±1/2⟩ + 0.13|±3/2⟩ + 0.09|±5/2⟩
7	303.5	0.6	1.1	15.6	0.31|±5/2⟩ + 0.20|±7/2⟩ + 0.19|±3/2⟩ + 0.14|±9/2⟩ + 0.09|±11/2⟩
8	435.8	0.1	0.1	19.3	0.21|±1/2⟩ + 0.19|±3/2⟩ + 0.17|±7/2⟩ + 0.17|±5/2⟩ + 0.16|±9/2⟩

Table S6. Computed energies levels (the ground state is set at zero), component values of the Lande factor *g* and wavefunction composition for each M_J state of the ground-state multiplet for Dy_2 center in **[Dy_2]**.

	E (cm^{-1})	g_x	g_y	g_z	WFT
1	0.00	< 0.1	< 0.1	19.4	0.93|±15/2⟩
2	132.0	0.4	0.6	15.6	0.75|±13/2⟩ + 0.11|±7/2⟩ + 0.09|±11/2⟩
3	206.4	1.5	2.1	11.0	0.34|±11/2⟩ + 0.23|±9/2⟩ + 0.15|±5/2⟩ + 0.10|±3/2⟩ + 0.10|±7/2⟩
4	242.7	0.6	1.3	16.4	0.49|±11/2⟩ + 0.20|±13/2⟩ + 0.11|±7/2⟩
5	291.0	0.0	1.8	10.6	0.63|±9/2⟩ + 0.15|±7/2⟩
6	355.2	6.5	5.5	3.2	0.44|±7/2⟩ + 0.23|±5/2⟩ + 0.13|±1/2⟩ + 0.13|±3/2⟩
7	416.1	2.6	3.6	12.0	0.42|±5/2⟩ + 0.39|±3/2⟩ + 0.10|±1/2⟩
8	467.6	0.6	2.2	17.9	0.60|±1/2⟩ + 0.30|±3/2⟩

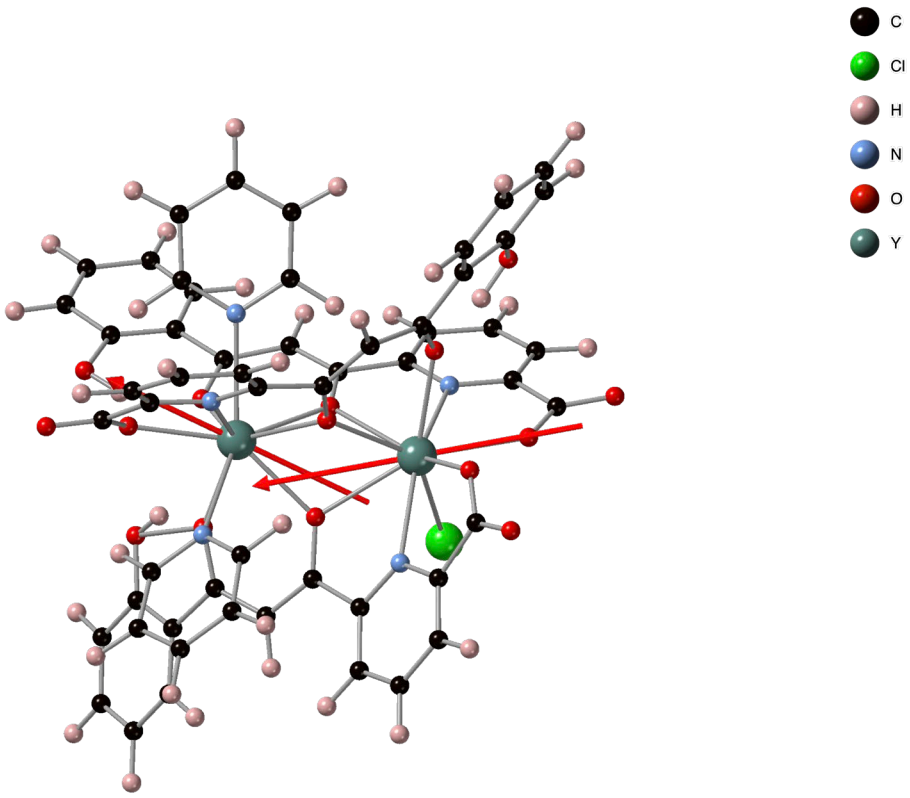

Figure S13. Anisotropy axes of the Dy(III) ions in **[Dy$_2$]**. The angle δ between the anisotropy axes of the two Dy ions $\overrightarrow{z_1}$ and $\overrightarrow{z_2}$ was obtained from the scalar product between the two corresponding vectors using the expression: $\delta = \cos^{-1}\left(\frac{\overrightarrow{z_1}\cdot\overrightarrow{z_2}}{\|z_1\|\|z_2\|}\right)$.

3. Numerical simulations of the magnetic flux generated by [Dy_2] arrays deposited onto micro-SQUID sensors.

Here we describe how to estimate the total flux that a given **[Dy_2]** molecular deposit, generates into the micro-SQUID pick-up coil. Assuming that each molecule can be approximated as point-like magnetic moment $\vec{\mu}$, induced by the excitation magnetic field, the flux it generates can be calculated as [3]:

$$\Phi = \frac{\vec{\mu} \cdot \vec{B}_{\mathrm{s}}}{i_{\mathrm{s}}}$$

Where $\vec{B}_{\mathrm{s}}$ is the magnetic flux created at the sample position by a current i_{s} circulating through the secondary coil. The induced magnetic moment, on the other hand, is determined by the linear magnetic susceptibility χ and by the magnetic field $\vec{H}_{\mathrm{p}}$ created by a current i_{p} circulating through the primary coil, resulting in $\vec{\mu} = \chi \vec{H}_{\mathrm{p}}$. The flux per unit of magnetic field is then given by:

$$\frac{\Phi}{H_{\mathrm{p}}} = \frac{i_{\mathrm{p}}}{B_{\mathrm{p}}} \frac{\chi}{i_{\mathrm{s}} i_{\mathrm{p}}} \vec{B}_{\mathrm{s}} \cdot \vec{B}_{\mathrm{p}}$$

Here, $\frac{B_{\mathrm{p}}}{i_{\mathrm{p}}}$.= 10^3 G/A is the average magnetic flux created at the sample position by unit of current in the primary coil.

The molecules are distributed over the inner surface of the secondary coil. To calculate the total flux, we can divide the sample into N_{cell} cells and sum over the magnetic flux created by each cell i:

$$\frac{\Phi_{\mathrm{TOT}}}{H_{\mathrm{p}}} = \frac{i_{\mathrm{p}}}{B_{\mathrm{p}}} \frac{N_{\mathrm{mol}} \chi'_{\mathrm{mol}}}{i_{\mathrm{s}} i_{\mathrm{p}}} \frac{1}{N_{\mathrm{cell}}} \sum_{i}^{N_{\mathrm{cell}}} \vec{B}_{\mathrm{s},i} \cdot \vec{B}_{\mathrm{p},i}$$

Here, N_{mol} is the number of moles of sample and χ'_{mol} is the molar susceptibility in cgs units, that we approximate by the simplest expression for a paramagnetic spin with a single relaxation time τ

$$\chi'_{\mathrm{mol}} = \frac{\chi_T}{1 + (\omega\tau)^2}$$

where χ_T is the equilibrium susceptibility. In our calculations, we set it equal to the Curie-Weiss law that describes the response of bulk **[Dy_2]** (see Figs. 2 and S8, and Eq. (1) in the main text), i.e.

$$\chi_T = \frac{2N_A g_{\mathrm{eff}}^2 S(S+1)\mu_B^2}{k_B(T-\theta)}$$

with

$$g_{\mathrm{eff}} = 11.2;\ S = \frac{1}{2};\ \theta = -0.067\ K$$

For the relaxation time, we use the Arrhenius law

$$\tau = \tau_0 exp\left({}^{U}/_{k_B T}\right)$$

And the parameter *U* and τ_0 found for each **[Dy_2]** sample (see Fig. 5 in the main text).

In order to determine Φ_{TOT}, the magnetic fields $\vec{B}_{\mathrm{s},i}$and $\vec{B}_{\mathrm{p},i}$ generated by the primary and secondary loops of the micro-SQUID susceptometer are estimated numerically using the 3D-MLSI software [4]. It allows calculating the magnetic flux created by the supercurrent distribution in a superconducting microcircuit with arbitrary shape. We use the actual dimensions of the primary and secondary coils as shown in Fig. S13a and the information on the sample geometry obtained from AFM experiments. The resulting position-dependent molar coupling is given in Fig. S14b in units of Φ_0 mol/emu. The total flux can be then obtained as:

$$\frac{\Phi_{\mathrm{TOT}}}{H_p} = \chi_{\mathrm{mol}} \sum_{i}^{N_{\mathrm{cell}}} \text{Molar Coupling}_{\,i}$$

Notice that the 2D map in Fig. 3 of the main text shows the position dependent coupling in units of Φ_0/emu. As can be seen in this figure as well as in panel b of Fig. S14, molecules located close to the pick-up coil contribute most to the net flux.

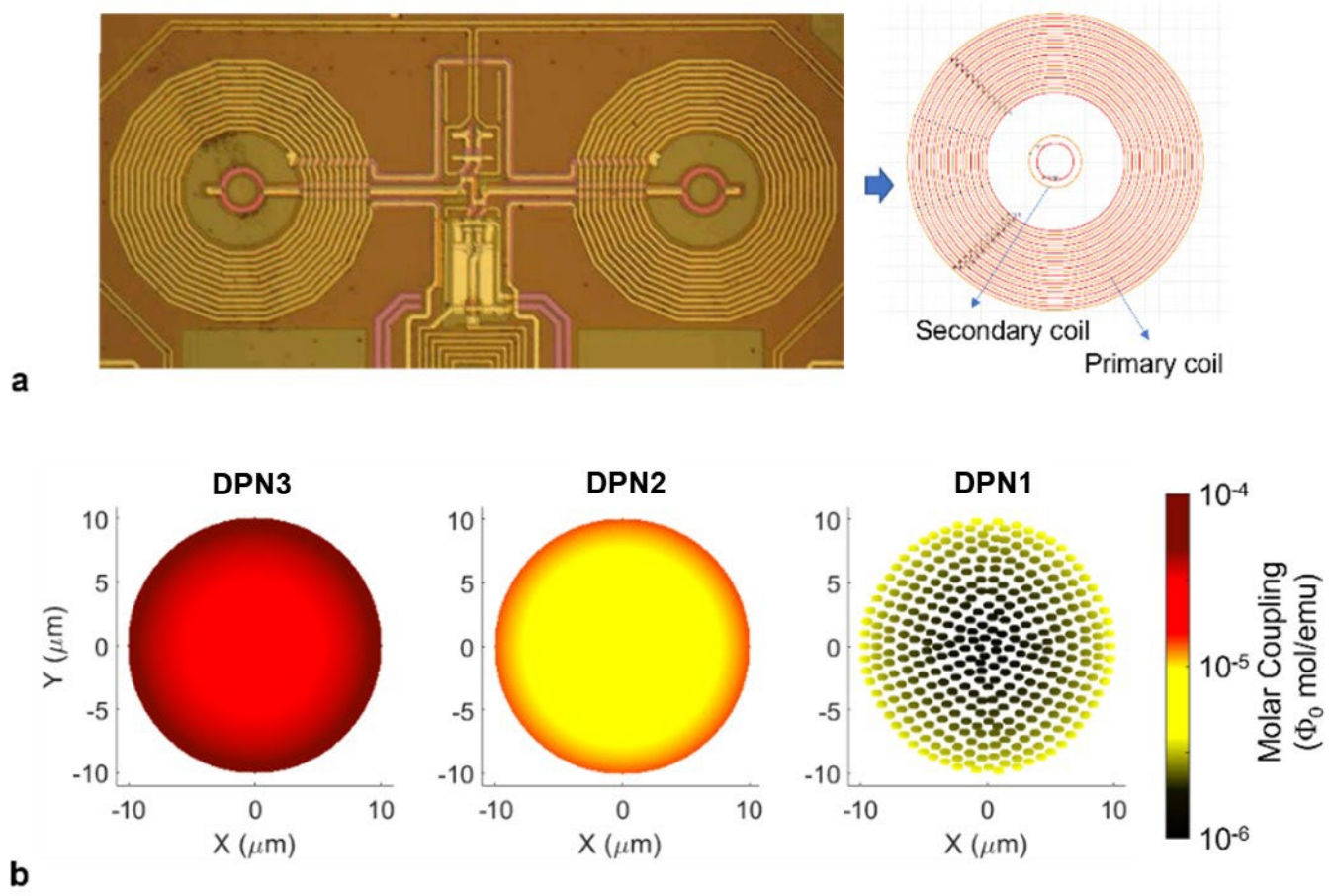

Figure S14: a) Left panel: optical image of the superconducting coils that form the micro-SQUID susceptometer. Right panel: circuit simulated with the 3D-MLSI software. b) Spatial distribution of the molar coupling for three **[Dy_2]** molecular deposits.

4. References

[1] K. S. Cole and R. H. Cole, *J. Chem. Phys.*, 1941, **9**, 341
[2] S. Stoll and A. Schweiger, *J. Magn. Reson.*, 2006, **178**, 42-55
[3] M. J. Martínez-Pérez, B. Müller, D. Schwebius, D. Korinski, R. Kleiner, J. Sesé, and D. Koelle, *Supercond. Sci. Technol.*, 2017, **30**, 024003
[4] M. M. Khapaev, M. Y. Kuprianov, E. Goldobin, and M. Siegel, *Supercond. Sci. Technol.*, 2002, **16**, 24